Electrification and Lightning in Idealized Simulations of a Hurricane-Like Vortex Subject to Wind Shear and Sea Surface Temperature Cooling

ALEXANDRE O. FIERRO

Cooperative Institute for Mesoscale Meteorological Studies, University of Oklahoma, and NOAA/OAR/National Severe Storms Laboratory, Norman, Oklahoma

EDWARD R. MANSELL

NOAA/National Severe Storms Laboratory, Norman, Oklahoma

(Manuscript received 22 September 2016, in final form 22 March 2017)

ABSTRACT

Relationships between intensity fluctuations, cloud microphysics, lightning variations, and electrical structures within idealized tropical cyclones are investigated with the cloud-resolving Collaborative Model for Multiscale Atmospheric Simulation (COMMAS). An initial strong tropical cyclone is subjected to either steady-state control conditions (CTRL), increased wind shear (SHEAR), or a reduction in sea surface temperature (SST).

In CTRL, nearly all the lightning (>95%) occurred in the outer region ($100 < r \leq 300$ km) and was overall very episodic in the inner core ($r \leq 100$ km), consistent with observations. The inner-core updrafts were weaker and experienced greater depletion of cloud water by warm rain processes, which, in contrast to the deeper updrafts in the rainband convection, reduced the mixed-phase cloud depth and confined the bulk of the charging and lightning initiations to lower levels.

Notably, larger flash rates were produced in the asymmetric inner core of the SHEAR case, with the majority of the flashes located in the downshear left quadrant, consistent with prior observational works. In contrast to CTRL, the more vigorous inner-core convection in SHEAR resulted in the formation of a prominent negative charge region and enhanced production of negative ground flashes.

With a nearly identical filling rate as SHEAR, the introduction of cooler sea surface temperature in the SST case caused lightning activity to fade rapidly in both the inner core and rainbands.

1. Introduction

In the last few decades, several observational studies employing primarily cloud-to-ground (CG) flash data within tropical cyclones (TCs) have established some associations between trends in lightning activity in different regions of the TC and intensity fluctuations (e.g., Lyons et al. 1989; Samsury and Orville 1994; Molinari et al. 1994, 1999; Orville and Coyne 1999; Cecil and Zipser 2002; Kelley et al. 2004; Shao et al. 2005; Squires and Businger 2008; Price et al. 2009; Thomas et al. 2010; Abarca et al. 2011; DeMaria et al. 2012; Bovalo et al. 2014; Stevenson et al. 2016). Because of the strong tie between lightning, deep moist mixed-phase convection, and intensity changes in many observed TCs, it is critical to augment our understanding of the relationships between intensity evolution and notable changes in lightning distribution within selected regions of the TC. This is particularly relevant given the recent successful launch of the Geostationary Operational Environmental Satellite R series (GOES-R), which will continuously monitor total lightning [CG plus intracloud (IC) flashes] over wide oceanic areas by means of the Geostationary Lightning Mapper instrument (GLM; Goodman et al. 2013). This study is an attempt to broaden our understanding on this topic by analyzing the electrification and lightning in idealized cloud-scale TC simulations.

Intensity changes and electrification within TCs are physically tied to transient, cloud-scale moist convective processes (MacGorman et al. 1989; MacGorman and Rust 1998; Anthes 2003; Hendricks et al. 2004; Montgomery et al. 2006; Nolan et al. 2007; Guimond

Corresponding author: Alexandre O. Fierro, alex.fierro@noaa.gov

DOI: 10.1175/JAS-D-16-0270.1

et al. 2010; Fierro and Reisner 2011; Fierro et al. 2015). The relationships between CG lightning activity and TC intensity change, however, are subject to ongoing debate, with the majority of studies suggesting that bursts in CG activity in the inner core precede intensification, while a few other studies (Thomas et al. 2010; DeMaria et al. 2012) have found that similar increases were coincident with the weakening of the TC. DeMaria et al. (2012) proposed that increased CG lightning activity in the outer region in the direct path of the TC's inner core may be a better surrogate for TC intensification, as this would be indicative of environmental conditions favorable for (electrified) deep moist convection ahead of the track of the TC. Perhaps partially reconciling this disagreement, Molinari et al. (1999) suggested that, given an increase in CG lightning in the inner core of the TC, subsequent weakening or intensification is contingent upon whether the TC is rapidly deepening or weakening, respectively, at the time of the lightning. CG flashes were emphasized by these studies because the lightning data were obtained from ground-based very-low-frequency networks, such as the World Wide Lightning Location Network (WWLLN; Abarca et al. 2011), which are unable to detect the weaker-amplitude radio emissions from the vast majority of IC flashes.

A three-dimensional analysis of CGs and of a class of high-current IC discharges within three major hurricanes revealed that intensification periods coincided better with episodic eyewall IC bursts than CGs alone (Fierro et al. 2011). In Hurricane Rita (2005), IC bursts were associated with distinct convective events rotating around the eye and with an aggregate increase in discharge heights. They also found that, in contrast to CGs, the evolution of the spatial distribution of ICs could help in identifying differences in convective regimes, particularly within the inner core of the TC. This more systematic association between deep convection and ICs is consistent with previous findings based on observations of total lightning within continental deep convective storms: in contrast to CGs, IC discharges exhibit a noticeably more robust relationship with convective vigor (volume of updraft $> 10\,\mathrm{m\,s^{-1}}$) and with bulk microphysical storm quantities, such as volume of graupel and 30-dBZ echo volume (e.g., MacGorman et al. 1989; Williams 1995; Lang and Rutledge 2002; Wiens et al. 2005; Schultz et al. 2011).

Few modeling studies on cloud-scale electrification processes within TCs have been conducted so far either for idealized cases (Fierro et al. 2007) or real cases (Fierro and Reisner 2011; Fierro et al. 2013, 2015). The reader is invited to consult Fierro et al. (2015) for an up-to-date review on the main findings of these modeling works.

The first study attempting to explicitly model cloud-scale electrification processes within TCs (Fierro et al. 2007) was able to reproduce their basic observed spatial lightning pattern (e.g., Molinari et al. 1999; Orville and Coyne 1999; Cecil and Zipser 2002; Cecil et al. 2002; Abarca et al. 2011; Stevenson et al. 2016), consisting of two distinct relative maxima in lightning activity: the first in the outer rainbands and a second in the inner core. Observations from the aforementioned investigators, however, showed a systematic larger maximum in the outer rainbands, indicating that the simulation of Fierro et al. (2007) overestimated the fraction of total lightning (and, hence, axisymmetric updraft speed and graupel content) in the inner core. Follow-on modeling studies from the same authors attempted to simulate real cases utilizing either finer grid spacing, more sophisticated microphysics, or the assimilation of real data (radar and lightning), but their simulations consistently overestimated total lightning activity in the inner core of the TC.

Using noninductive charging schemes based on the laboratory work of Saunders and Peck (1998, hereinafter SP98), these modeling studies revealed that, overall, the gross charge structure of the deeper convective elements within the simulated TC resembled a normal tripole, which consists of a main midlevel negative charge region located between upper and lower regions of positive charge (Williams 1989). Akin to simulations of continental thunderstorms, it was found that negative noninductive charging of graupel pellets dominated at midlevels, followed by relatively weaker positive noninductive charging on graupel at lower levels. The charging configuration, however, is relatively sensitive to the noninductive charging scheme employed (e.g., Mansell et al. 2005; Kuhlman et al. 2006; Fierro et al. 2006).

To build upon prior modeling works, this study will explore how the electrical structure of an initially strong hurricane-like vortex (category 3 or greater on the Saffir–Simpson scale) evolves when the ambient wind shear is increased or when the sea surface temperature is reduced.

2. Numerical model

This study makes use of the Collaborative Model for Multiscale Atmospheric Simulation (COMMAS; Wicker and Wilhelmson 1995; Coniglio et al. 2006). The equation set is based on Klemp and Wilhelmson (1978). The simulations employed the NSSL two-moment, four-ice-category bulk microphysics scheme (Mansell et al. 2010; Ziegler 1985; Mansell and Ziegler 2013). This scheme predicts the mass mixing ratio and number

concentration of six hydrometeor species (cloud droplets, rain, graupel, hail, cloud ice, and snow) together with graupel and hail particle densities. In this set of simulations, both the cloud condensation nuclei (CCN) number concentration and the number of activated CCN ($N_{\mathrm{CCN},a}$) are predicted. The hail category was turned off because large, high-density ice particles produced by wet growth of graupel are not expected in tropical cyclones. Initial tests also showed virtually no hail production.

The two-moment microphysics scheme is nearly identical to the NSSL scheme within version 3.8 of the Weather Research and Forecasting (WRF) Model with the Advanced Research WRF (ARW) dynamic solver (Skamarock and Klemp 2008). A few relevant differences from the version used in Fierro et al. (2015) are described below.

The NSSL microphysics scheme explicitly calculates condensation rates, which can result in some residual supersaturation S_w, especially when droplet concentrations are low (e.g., Khain et al. 2012; Mansell and Ziegler 2013). Most other bulk schemes use a saturation adjustment procedure, but Khain et al. (2015) noted that this tended to reduce sensitivity to CCN concentration in a tropical cyclone simulation. As noted in Mansell and Ziegler (2013), most of the CCN are activated within 1 km or so above cloud base. The TC environment is assumed to have typical maritime CCN concentrations on the order of 100 cm^{-3}, which in Mansell and Ziegler (2013) resulted in maximum S_w values on the order of 10% for a small isolated cell. Preliminary TC simulations, however, produced very large S_w values (>50%) over deep regions within the eyewall convection. These were attributed to extreme droplet scavenging by rain, leaving too few droplets for effective condensation in the updrafts. Although there are no reliable observations of supersaturation in eyewalls, these values seemed unreasonably large and would potentially result in the activation of more numerous small cloud nuclei (e.g., Khain et al. 2012). To mitigate this issue, the droplet renucleation term in this work was reformulated as an extension of the Phillips et al. (2007) strategy that tracks both the number of activated nuclei $N_{\mathrm{CCN},a}$ and the background CCN concentration N_{CCN} (where N_{CCN} is advected but not decremented). As formulated, the Phillips et al. (2007) scheme also suffered from large S_w in these conditions, so an assumption similar to that of Khain et al. (2012) was made that sufficiently high supersaturations should continue to nucleate a few additional small aerosols. When cloud water already exists, the number of newly nucleated droplets C_N is given by

$$C_N = \begin{cases} \dfrac{1}{\Delta t}\max(C_{N,\mathrm{cb}} - N_{\mathrm{CCN},a}, 0) & \text{for} \quad N_{\mathrm{CCN},a} \le 0.9 N_{\mathrm{CCN}} \\ \dfrac{1}{\Delta t}\max(N_{\mathrm{CCN}} S_w^k - N_{\mathrm{CCN},a}, 0) & \text{for} \quad N_{\mathrm{CCN},a} > 0.9_{\mathrm{CCN}} \quad \text{and} \quad S_w \le 1\% \\ \dfrac{c_{s1}}{\Delta t}\max[N_{\mathrm{CCN}}\min(2, c_{s2} S_w^k) - N_{\mathrm{CCN},a}, 0] & \text{for} \quad N_{\mathrm{CCN},a} > 0.9 N_{\mathrm{CCN}} \quad \text{and} \quad S_w > 1\% \end{cases}, \tag{1}$$

where $C_{N,\mathrm{cb}}$ is the Twomey (1959) cloud-base value [Eq. (A7) in Mansell et al. (2010)]:

$$C_{N,\mathrm{cb}} = \frac{1}{\Delta t} 10^6 (10^{-6} N_{\mathrm{CCN}})^{2/(k+2)} \left[\frac{1.63 w^{3/2}}{kB(3/2, k/2)} \right]^{k/(k+2)}, \tag{2}$$

where N_{CCN} is the assumed CCN concentration, k is the aerosol activation spectrum exponent (here, $k = 0.6$), w is the updraft speed, and B is the complete beta function. The supersaturation with respect to liquid water S_w is calculated from the model state after condensation and other microphysics rates have been applied. The constants c_{s1} and c_{s2} are tuning parameters that allow an extended weak response to very high S_w and for this study have values of 0.01 and 0.03, respectively. The scheme essentially reserves 10% of the CCN for activation at high S_w. An alternative future approach might try to limit accretion and autoconversion from reducing the droplet concentration below some threshold. The $N_{\mathrm{CCN},a}$ field is exponentially damped (time constant of 1 min) at grid points with no cloud droplets or ice crystals, which effectively restores CCN when air is cloud free. This is done because there is otherwise no source term for CCN, which tend to get depleted in the TC environment. The actual CCN field is only advected, and the depletion is counted by the separate activated CCN field ($N_{\mathrm{CCN},a}$).

Mansell et al. (2010) included a simple but weak process of ice crystal production by splintering of ice shells as drops freeze (Chisnell and Latham 1974). They assumed one splinter per frozen drop, but new observations and model results from Lawson et al. (2015) suggest a possibly much larger effect, where the number of splinter fragments N_f is proportional to the diameter

d of the freezing drops. From 1D spectral microphysics model simulations, they found an average relationship of $N_f = 2.5 \times 10^{-11} d^4$ using parameters that best reproduced the aircraft observations. The splinter fragments provided a feedback that accelerated the glaciation of rain drops, as seen in the observations. For the bulk microphysics, we applied this relationship to drop freezing both by internal nucleation (Bigg 1953) and by ice crystal capture. For both cases, the drop diameter d_r was taken to be the mean mass diameter of the newly frozen drops, and the mass of new ice crystals is 6.88×10^{-13} kg. Activation of this process notably increased the drop freezing rate by ice crystal capture. Drop–crystal interactions are limited to drops in the size distribution with $d_r > 150\,\mu$m that capture ice crystals with $d_i > 40\,\mu$m (and a mean diameter greater than $10\,\mu$m), so that smaller drops are still left to freeze via the Bigg process.

The noninductive charging scheme for graupel–ice collisions uses a rime accretion rate parameterization (RAR; SP98; Brooks et al. 1997) that is modified from Mansell et al. (2010) at lower temperature. The sharp drop in the critical RAR curve at low temperature was replaced with a cosine function for temperature $T < -23$°C to smoothly approach zero at −37°C (Fig. 1a). Likewise, the quadratic roll-off factor β [Mansell et al. 2005, Eq. (11)] was also replaced with a cosine function $\beta = 0.5\{1 + \cos[\pi(T - T_c)/(T_c - T_{\min})]\}$, where $T_c = -30$°C and $T_{\min} = -37$°C. These changes provide a smoother approach to zero charging at temperatures where cloud droplets are rapidly freezing. In this model, noninductive charging between graupel and snow is treated the same as graupel–ice owing to the lack of laboratory experiments. Inductive or polarization charging arising from rebounding collisions between graupel particles and cloud droplets following Ziegler et al. (1991) is also accounted for. Discharges are simulated by the three-dimensional stochastic branched lightning scheme of Mansell et al. (2002), and flashes are initiated based on the height-dependent electric field magnitude threshold E_{init} of Dwyer (2003) and scaled from standard air density ($\rho_0 = 1.225\,\text{kg m}^{-3}$): $E_{\text{init}} = 2.84 \times 10^5(\rho_{\text{air}}/\rho_0)$ V m^{-1}. The electric field is computed by a black box multigrid iterative solver (Dendy 1982, 1987). Drift and attachment of small atmospheric ions are explicitly treated (Chiu 1978; Mansell et al. 2005).

3. Experimental design

The horizontally homogeneous environment initially at rest was prescribed by a modified version of the tropical sounding used in Fierro et al. (2007) (Fig. 1b), which is a combination of the 0000 UTC 13 August 2004 Owen Roberts Airport, Grand Cayman Island, profile below 15 km MSL and, above it, the 0000 UTC 13 August 2004 Kingston, Jamaica, profile. This particular time and date were chosen because Hurricane Charley (2004) passed within 150 km of Grand Cayman Island.

The initial wind field of the vortex was prescribed following Rotunno and Emanuel (1987) as implemented in WRF-ARW (version 3.7), which assumes a vortex in gradient wind and hydrostatic balance. The bogusing scheme includes four main input parameters that control the size and strength of the initial vortex, namely, the maximum tangential wind, the radius of maximum wind (RMW), the vortex depth, and the radius of zero horizontal wind. To guarantee and hasten the development of a strong TC, the current simulations used a maximum tangential wind of 30 m s^{-1}, RMW = 100 km, a vortex height of 15 km, sea surface temperature of 27°C (e.g., Williams and Renno 1993), and a radius of zero wind of 700 km. With these coefficients, a realistic strong hurricane-like vortex (i.e., category 3 or greater on the Saffir–Simpson scale) was obtained after 24 h of integration (without electrification), which was used as the initial conditions for the three experiments analyzed in this study.

To help reduce the detrimental effects of compensating subsidence in the far field developing after long integrations on a finite-size domain, a Newtonian cooling term was applied in the simulations following Rotunno and Emanuel (1987). The equations of motion were integrated on an f plane with a constant assumed latitude of 25°. The wind-dependent drag coefficient C_d, which controls the magnitude of the bulk surface fluxes of heat and moisture, is parameterized following the observational work of Powell et al. (2003), wherein C_d levels off for horizontal wind speeds exceeding hurricane force (40 m s^{-1}). COMMAS does not include an ocean model or a longwave and shortwave radiation scheme.

The vertical grid has 60 levels, and the spacing stretches from 100 m at the lowest level to a maximum of 500 m above 8.25 km MSL, with the model top set at 22 km MSL. The horizontal dimensions of the domain are, in grid points, 450 × 450 (1600 × 1600 km^2). In the horizontal, the grid stretches geometrically from a finer mesh of 2.5 km within a 240 × 240 gridpoint (600 × 600 km^2) storm-centered subdomain to a coarser mesh of 5 km in the outer regions. The time step was set to 5 s with open lateral boundary conditions.

The first of three simulations is the control (CTRL), wherein the model solution at 24 h is integrated for an additional 30 h without any changes to the background environment, resulting in a nearly steady-state axisymmetric strong TC. The second experiment (SHEAR) is like CTRL but with the progressive introduction of deep (full tropospheric: 850–250 hPa) wind shear, assumed here to be unidirectional in the zonal direction, for

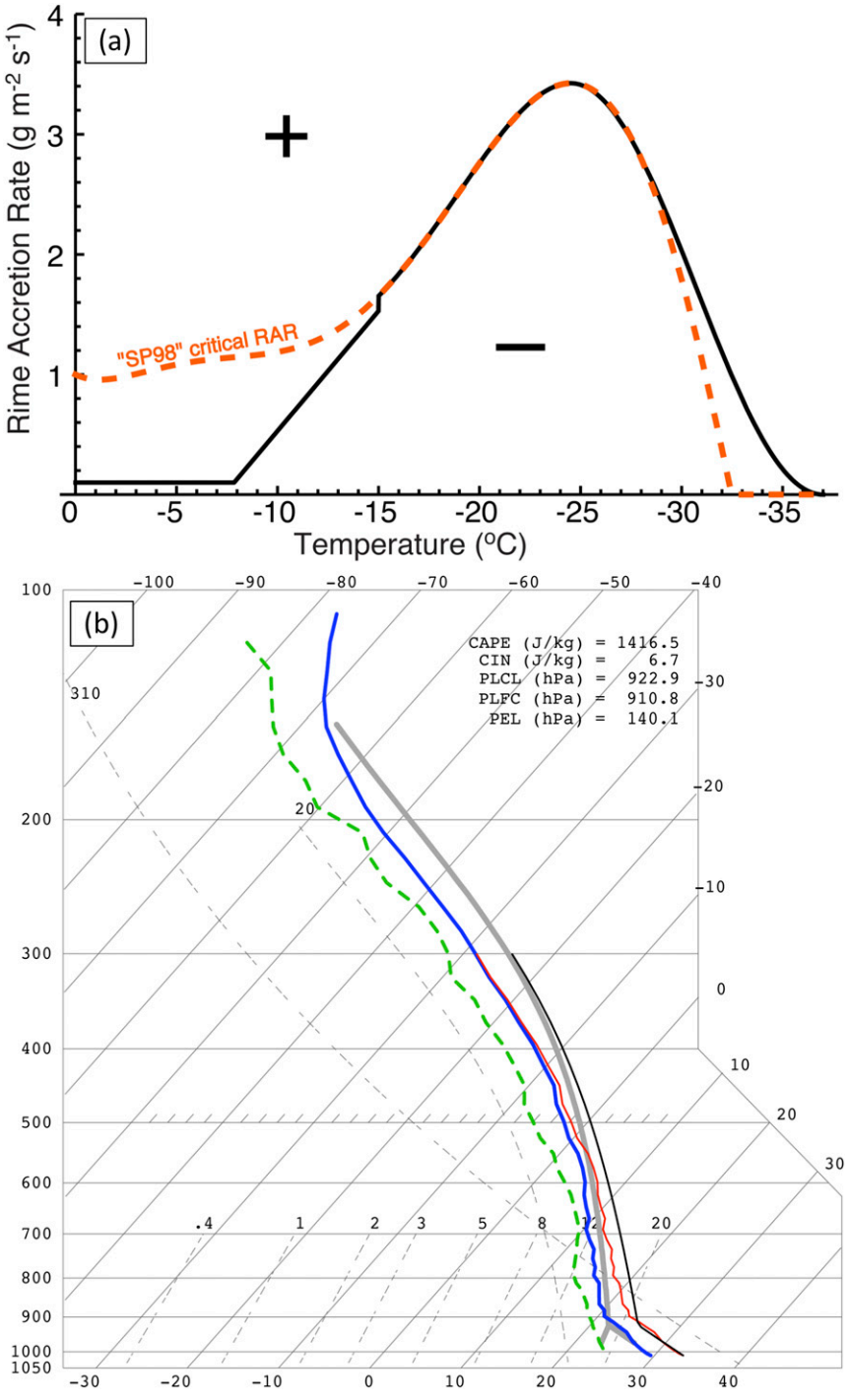

FIG. 1. (a) Plot of the noninductive charge separation sign-reversal curve used in this study (black curve), which is the same as in Mansell et al. (2010), except for the use of a cosine function to replace the polynomial for $-24° < T < -37°$C (see text). The original SP98 curve fit is shown as the dashed orange curve for reference. (b) Skew T–log$p$ plot of temperature (blue) and dewpoint (green) used to initialize the horizontally homogeneous environment in the simulations. The thick gray curve shows the lifted parcel from a 90-hPa-deep mixed layer extending from the surface, which is used to compute the sounding parameters shown on the top-right corner. The thin red and black curves are the virtual temperature profiles of the environment and the lifted parcel, respectively.

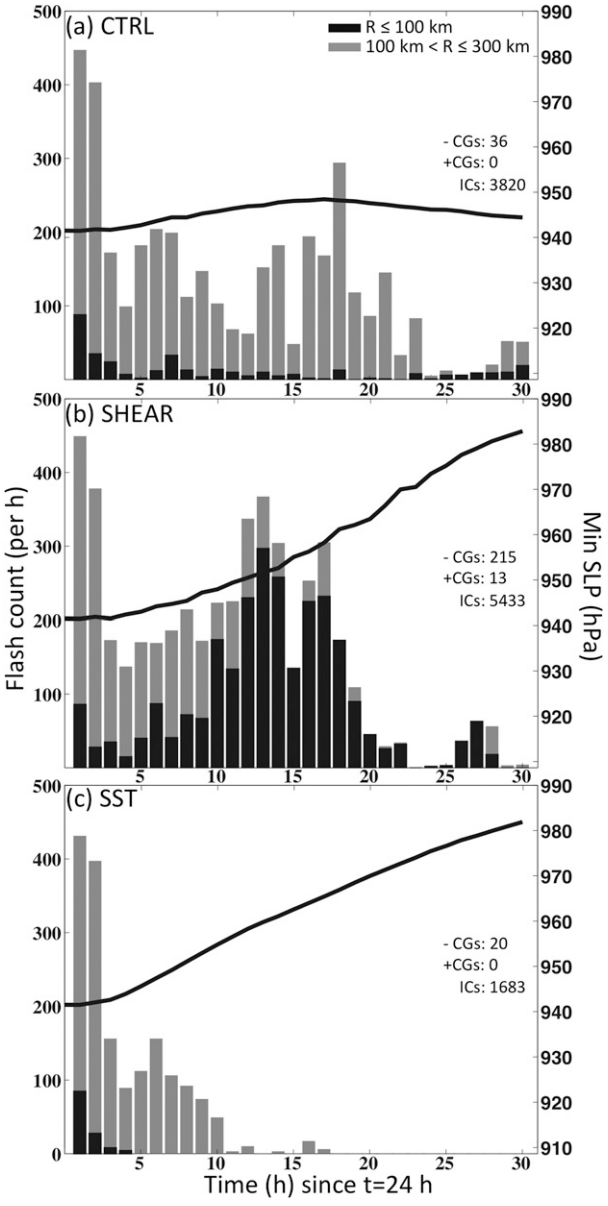

FIG. 2. Stacked bar charts of the time series of the hourly flash rates for (a) CTRL, (b) SHEAR, and, (c) SST on the native Cartesian grid. The flash rates were computed on prescribed storm-centered cylinders containing the rainband region (gray portion of each bar) and inner-core region (black portion of each bar). The inner-core rates include all flashes within a radius $r = 100$ km from the storm center. The lightning rates in the outer region include all flashes within $100 < r \leq 300$ km. The storm center is the gridpoint location with the minimum total pressure at the surface. The sum of the respective flash rates of the black and gray portions of each bar represents the "storm total" rate, which is shown on the Y axis (i.e., over the entire $r = 300$-km storm-centered cylinder mask). As a reference, the diagram also shows for each experiment the domain-integrated flash totals categorized by flash type and polarity, namely, ICs, negative CGs, and positive CGs. The time series also show the surface pressure trace (hPa) for each corresponding experiment as a solid black line. To facilitate comparison, the respective scale for the storm total flash rates (left axis) and the pressure trace (right axis) use the same upper and lower bounds for each experiment.

simplicity. The base-state substitution method of Letkewicz et al. (2013) was used to introduce a wind shear magnitude of $15\,\mathrm{m\,s^{-1}}$ in the U component of the wind field over the layer between $z = 1.5$ and 10.5 km. During the substitution, the base-state U component is set to negative values (easterly) from the surface up to $z = 1.5$ km and increases linearly to a positive value (westerly) until $z = 10.5$ km. The base-state U winds were adjusted linearly at each time step over the first 10 h of simulation and then maintained throughout the remainder of the simulation. The shear profile was adjusted to have a mean U wind of $0.5\,\mathrm{m\,s^{-1}}$ to keep the TC centered in the domain. Although this shear increase is admittedly large (Marks et al. 1992; Reasor et al. 2000, 2009; M. DeMaria 2016, personal communication), these values were chosen for faster development and computational efficiency. The third experiment (referred to as SST) simply decreases the homogeneous sea surface temperature from its initial value of 27°C to a final value of 22°C over the same time period as SHEAR, namely, during the first 10 h of simulation. The final SST, which is then maintained throughout the remainder of the simulation, was purposely set markedly below the threshold of 26°C for TC maintenance and development (e.g., Williams and Renno 1993) to simultaneously reduce computational burden and emphasize the main changes in TC structures. Full model fields were saved every hour. The mean storm motion in all simulations is relatively small ($\leq 2\,\mathrm{m\,s^{-1}}$), allowing the TC to remain reasonably close to the center of the domain and within the finer 2.5-km-resolution mesh.

Given the above experimental design, this study places emphasis on a steady-state strong TC and two weakening TC scenarios. These two particular weakening scenarios were investigated to illustrate the inherent challenge in relating changes in TC intensity to lightning activity, as both TCs exhibit similar filling rates while producing drastically different lightning behaviors. Because preliminary tests revealed that realistic simulations of intensifying TCs are somewhat challenging to achieve in the current idealized framework, such an endeavor is deferred to future work.

4. Results

In all three experiments, the analysis emphasizes systematic comparisons between two key regions of the TC on a storm-centered cylindrical grid: the inner core ($r \leq 100$ km) and the outer region ($100 < r \leq 300$ km). Because the flash (origin) density is a relatively discrete field, it was analyzed within the same respective storm-centered cylinders but still on the native grid (i.e., using a mask) to avoid truncation errors during

interpolation [as in Fierro et al. (2015)]. Following the definitions of Cecil et al. (2002), the outer region contains both the inner band region (characterized by a minimum in lightning) and the outer-rainband region (characterized by the maximum in lightning) of the TC. For simplicity, the terms "outer region" and "rainband region" will be used interchangeably throughout the manuscript. All altitudes are MSL.

a. Control simulation

As noted earlier, CTRL produces a steady-state, quasi-axisymmetric strong hurricane-like vortex exhibiting a lightning behavior and evolution consistent with those of observed TCs (e.g., Molinari et al. 1994, 1999; Cecil and Zipser 2002; Squires and Businger 2008; Fierro et al. 2011; Stevenson et al. 2016). The vast majority (i.e., ~91%) of the lightning within $r = 300$ km originates from the outer region (Fig. 2a). The simulation produced 36 CG flashes, all of which lowered negative charge, which is likely a large underestimate. In all simulations, many of the IC flashes that initiated at lower levels might be expected to have become CG flashes, but the coarseness of the grid and other biases related to the generation and resolution of the charge and potential structure may be inhibiting propagation all the way to the surface (Mansell et al. 2002, 2010). Hourly rainband lightning rates (Fig. 2a) had substantial variability, with total rates from as low as 10 flashes per hour (flashes h^{-1}) to a maximum near 450 h^{-1}. The inner-core region, in contrast, produced overall smaller rates never exceeding 100 flashes h^{-1}. About ~30% of the inner-core flashes are associated with small updrafts within r = 75–100 km that are connected to the outer bands and are therefore not directly associated with the eyewall convection. The factors behind this contrast in lightning evolution between the eyewall and rainband convection will be examined later in the section.

Note that, because the simulations assume a positive Coriolis parameter and the CTRL storm motion is westward, the right-front (rear left) quadrant is located to the northwest (southeast). About half of the inner-core lightning 30-h totals were produced in the right-front quadrant (Fig. 3). This is consistent with early modeling works (e.g., Shapiro 1983; Shapiro and Franklin 1999) highlighting that a translating TC usually has stronger boundary layer convergence in the right-front quadrant in the eyewall, relative to the TC motion. Most of the lightning produced in the outer region (i.e., ~43%) is in the rear-left quadrant of CTRL.

The accumulated hourly lightning flashes and the instantaneous radar reflectivity fields at z = 1 km at 9 (Fig. 4a) and 19 h (Fig. 4d) provide representative snapshots of the precipitation structure relative to the simulated lightning. Consistent with observations in mature hurricanes, radar reflectivity values seldom exceed 50 dBZ in the eyewall but are a more common occurrence in some of the isolated and often lightning-active convective cells within the rainbands. As anticipated from the initialization procedures, CTRL produces a persistent, nearly axisymmetric eyewall (Figs. 4a,d).

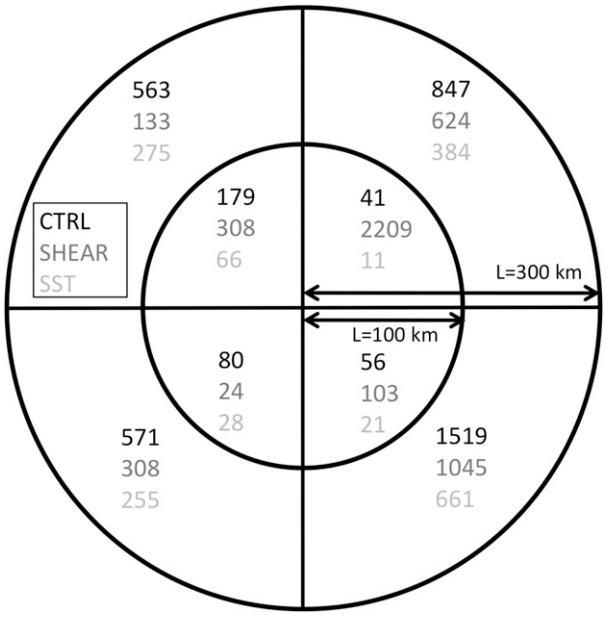

FIG. 3. Diagram showing the total number of flashes over the 30 h of simulation for CTRL (black), SHEAR (dark gray), and SST (light gray) within the inner-core and rainband regions divided by quadrants within the cylinders described in Fig. 2 (which are on the native Cartesian grid).

Complementing Fig. 4, a Hovmöller diagram of the column-total lightning channels and 4–7-km mean reflectivities (Fig. 5a) reveals a persistent eyewall with a radius of about 20 km early in the simulation, gradually widening to about 35 km by the end of the simulation. Figure 5a also highlights an outward shift of the lightning in the outer region with time, in line with a progressively widening eyewall and primary circulation. Lightning in the eyewall was generally well collocated with the maximum in 4–7-km layer-averaged reflectivity. This nearly unvarying horizontal reflectivity structure is a reflection of a nearly steady-state TC intensity as measured by the minimum surface pressure of about 945 hPa (Fig. 2a).

As in Fierro et al. (2015), the analysis includes time–height volumes of selected variables. The volumes for a given variable A (interpolated onto the cylindrical grid) are computed as follows. At each level in the model, an algorithm counts instances when A exceeds a fixed threshold (e.g., 0.5 g kg^{-1} for graupel mass). The total count at each

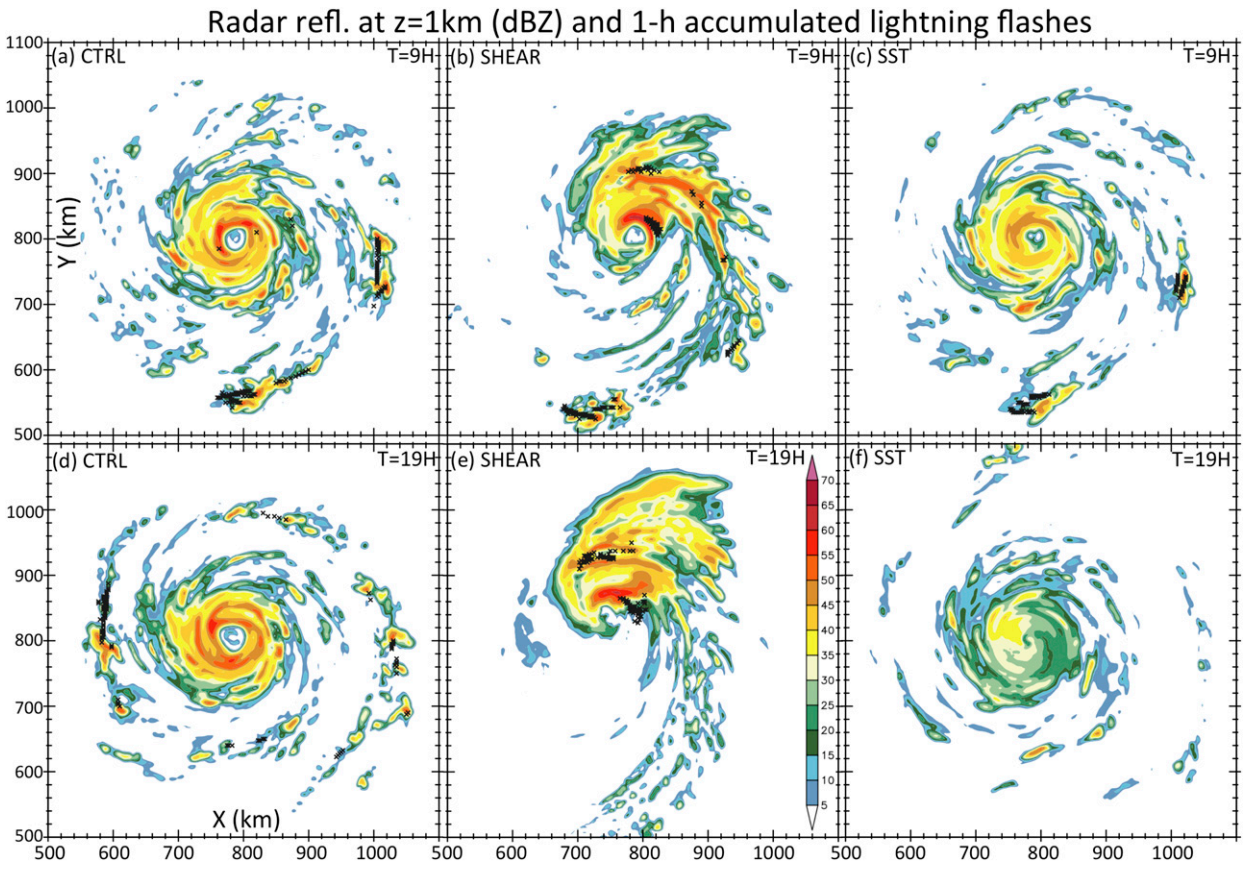

FIG. 4. Horizontal cross sections of simulated radar reflectivity fields at $z = 1$ km MSL overlaid with lightning initiation locations (black crosses) for (a) CTRL, (b) SHEAR, and (c) SST at 9 h into the simulation. (d)–(f) As in (a)–(c), respectively, but at 19 h.

level is then scaled (multiplied) by the average volume of the grid cell (because of the stretched grid). When the volumes were computed with the actual (i.e., height varying) volume of the grid cell, the results were quantitatively very similar. From this definition, the volumes thus provide information on the bulk content combined with the spatial and vertical extent of a variable within a predefined region of the system of interest.

Consistent with larger flash rates in the outer region (compared to the inner core) in the first 24 h of simulation (Figs. 2a) and, hence, larger total channel volumes (Figs. 6a, 7), the CTRL TC outer region also exhibits systematically larger $0.1\,\mathrm{nC\,m^{-3}}$ total space charge magnitude volumes (Fig. 8a), $5\,\mathrm{m\,s^{-1}}$ updraft volumes (Fig. 9a), $0.5\,\mathrm{g\,kg^{-1}}$ graupel volumes (Fig. 10a) and snow plus cloud-ice volumes (not shown). The total channel volumes can be viewed as a measure of the total electrical discharge activity by considering flash size [volumetric extent (Fierro et al. 2015)]. During the first 24 h of simulation, the total channel volumes in the outer region are nearly an order of magnitude larger than in the inner core (Figs. 6a, 7) and generally locate at significantly higher altitudes than in the inner core: for example, the 100-$\mathrm{km^3}$-volume contour in the inner core seldom exceeds 10-km altitude, in contrast to the outer region, where this contour often exceeds 16 km (Fig. 6a). This tendency for the outer region to exhibit systematically larger volumes at higher altitudes is also seen for the $0.1\,\mathrm{nC\,m^{-3}}$ total space charge magnitude volumes (Fig. 8a), $5\,\mathrm{m\,s^{-1}}$ updraft volumes (Fig. 9a), and $0.5\,\mathrm{g\,kg^{-1}}$ graupel volumes (Fig. 10a). The lightning channels in the inner core, however, generally occur at lower levels than in the outer region, a behavior also seen for the $5\,\mathrm{m\,s^{-1}}$ updraft volumes (Fig. 9a) and, arguably, for the $0.1\,\mathrm{nC\,m^{-3}}$ total space charge magnitude volumes (Fig. 8a).

Some of the earlier results become clearer by partitioning the channels by polarity in the inner-core and outer regions (Fig. 7). While the gross vertical arrangement of lightning channel polarity is generally consistent throughout the TC, namely, a middle layer containing mainly positive channels between 7- and 10-km altitude between two layers containing predominantly negative channels, some differences remain noteworthy. Consistent with moderate ($\sim 5\,\mathrm{m\,s^{-1}}$) updrafts generally

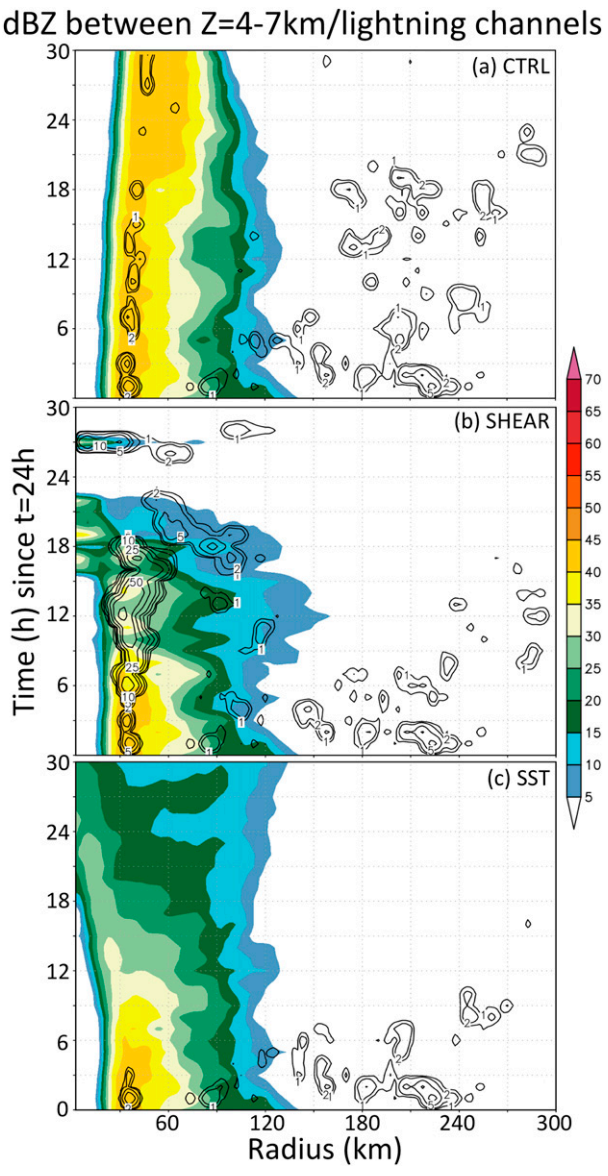

FIG. 5. Storm-centered Hovmöller diagrams of the radar reflectivity fields averaged within the $z = 4$ and 7 km MSL layer and the total number of lightning channels (sum of positive and negative channels in the entire column; black contours) for (a) CTRL, (b) SHEAR, and (c) SST.

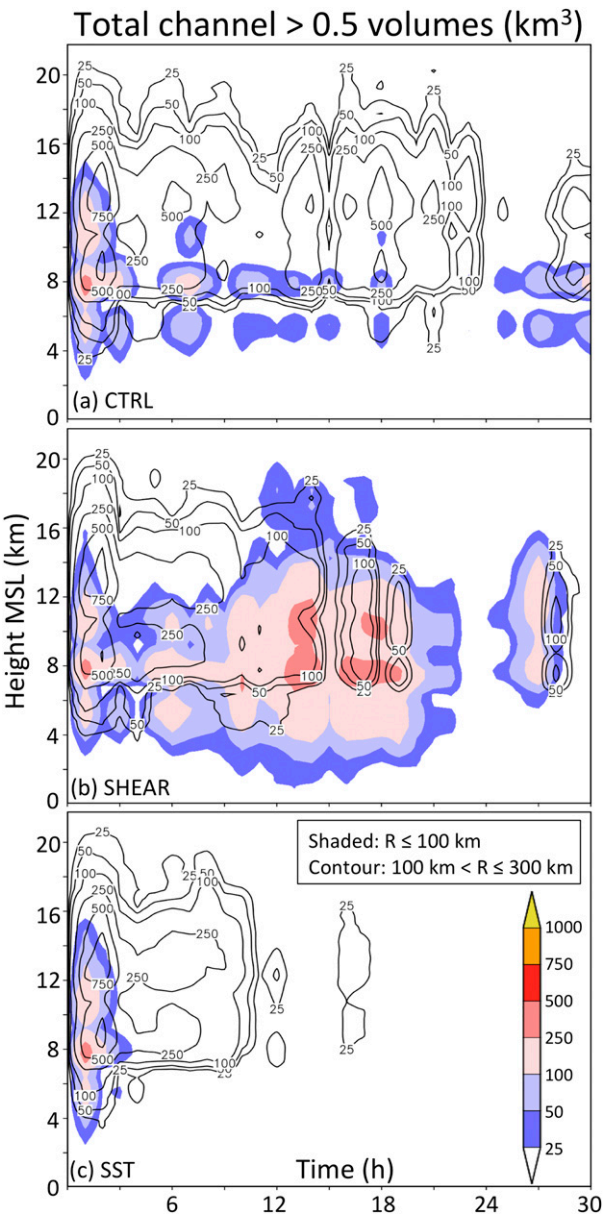

FIG. 6. Time–height plot of total lightning channel (>0.5) volumes (km^3 per average level) for (a), CTRL, (b) SHEAR, and (c) SST. All time–height volume plots herein were computed from model data interpolated on a storm-centered cylindrical grid to better isolate the inner-core region (cylinder of radius $r = 100$ km) and outer region (cylinder volume within $100 < r \leq 300$ km), respectively. As in Fierro et al. (2015), the volumes for a given variable A interpolated on the cylindrical grid are computed using the following procedures: At each level in the model, an algorithm counts instances when A exceeds a fixed threshold (here 0.5). The total count at each level is then scaled (multiplied) by the average volume of the grid cell (because of the stretched grid). Shaded areas show the volumes for the inner core, and, similarly, the contours show the volumes for the rainband region. The legend for color shading is shown in (c). To facilitate comparison, the contour levels are the same as for the shading.

located at lower levels in the inner core, the negative channel volumes at lower levels (below 6 km) are significantly larger in the inner core. Similarly, the outer region has deeper 5 m s^{-1} updrafts (Fig. 9a) and larger negative channel volumes at upper levels (Fig. 7b, at 11–18-km altitude).

Lightning channels generally carry the opposite polarity of charge to the ambient net charge; thus, the vertical arrangement of lightning channel polarity in Fig. 7 also reveals that the gross charge structure in the

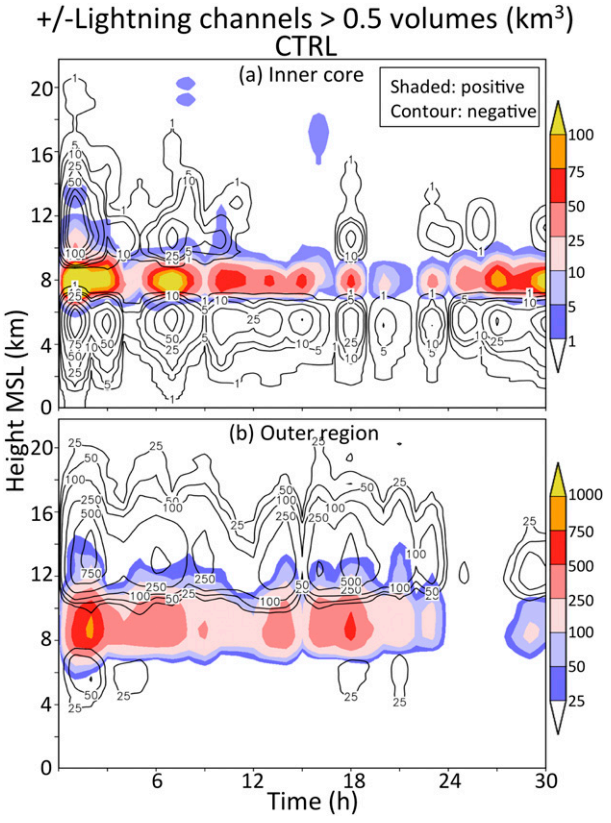

FIG. 7. As in Fig. 6, but for the (a) inner-core and (b) outer regions in the CTRL run separated by polarity. Note the different scales used for the inner-core and outer regions, which are shown on the right of each respective panel.

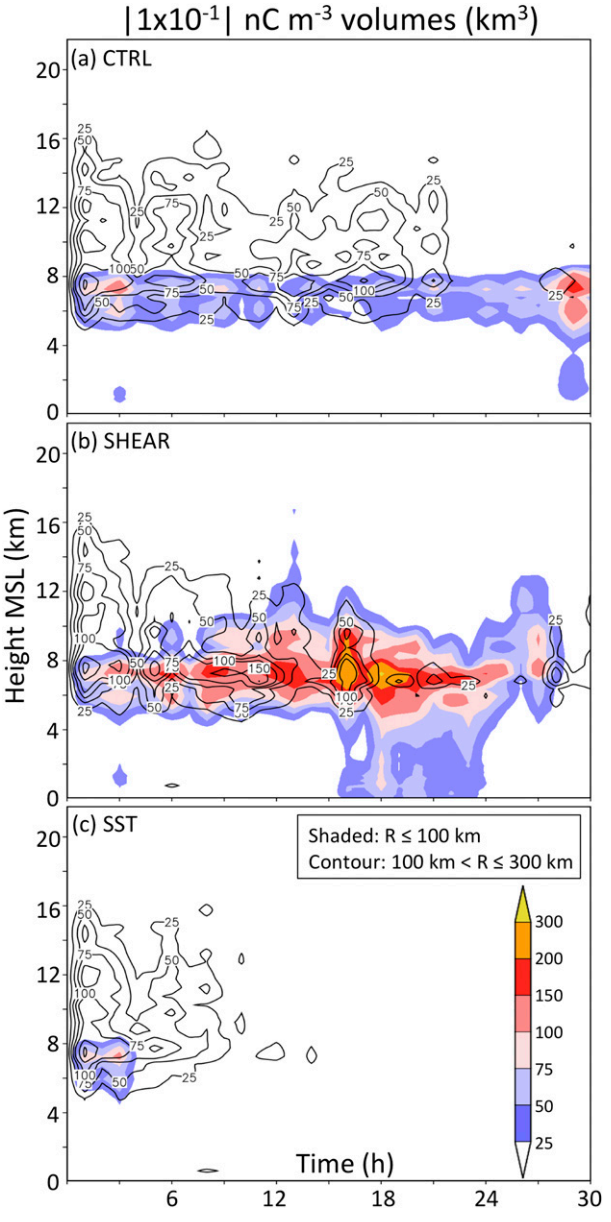

FIG. 8. As in Fig. 6, but for the volumes (km^3 per average level) of the sum of positive and negative space charge magnitude exceeding 0.1 $nC\ m^{-3}$.

majority of the convective cells within the TC resembles a normal tripole (e.g., Williams 1989) consistent with lightning observations in mature TCs (Black and Hallett 1999; Fierro et al. 2011) and prior TC modeling studies using SP98 (Fierro et al. 2007, 2013, 2015). Because lightning rates (Fig. 2a) and volumes (Figs. 6a, 7) correlate with volumes of charge density (Fig. 8a), this tripole is characterized by a main midlevel negative charge region underneath a main upper positive charge region coupled with a relatively weaker positive charge region at lower levels below about 7 km. A tripole wherein the lower positive charge region has more lightning activity than the upper positive charge region is referred to as a "bottom heavy" tripole by Mansell et al. (2010).

Because noninductive charging requires the simultaneous presence of ice hydrometeors and supercooled cloud water, it is also relevant to examine the evolution of cloud water volumes (>0.1 $g\ kg^{-1}$; Fig. 11a) above the freezing level (~4.5–5 km). The higher values of cloud droplet volumes in the outer region of CTRL (Fig. 11a) compared to the inner region (up to about 24 h) indicate a greater total convective area, which is consistent with greater total flash rates in the outer region.

The time–height diagrams of the domain-integrated 1-min net graupel charging rates (Fig. 12a) show that, overall, positive charging occurs between 6.5 and 8 km with negative charging above that over a deeper layer, between 8 and 11 km. Given that positive charge is acquired by the lighter ice crystals during the negative noninductive collisional charging with graupel between 8 and 10.5 km, positive charge will be lofted by updrafts

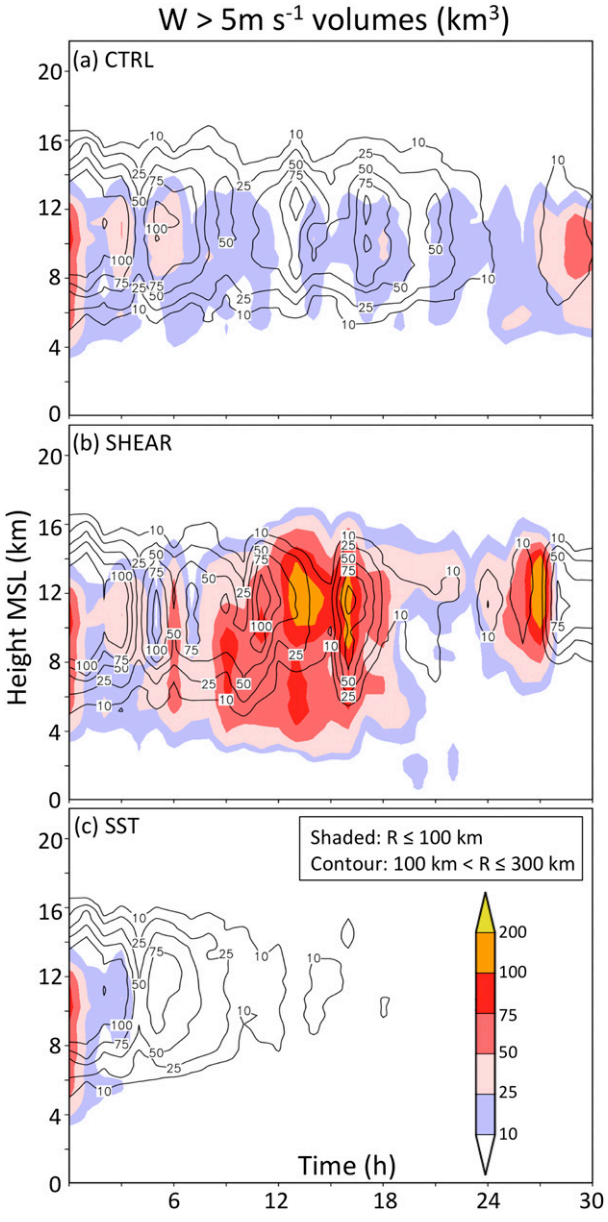

FIG. 9. As in Fig. 6, but for the 5 m s^{-1} updraft volumes (km^3 per average level).

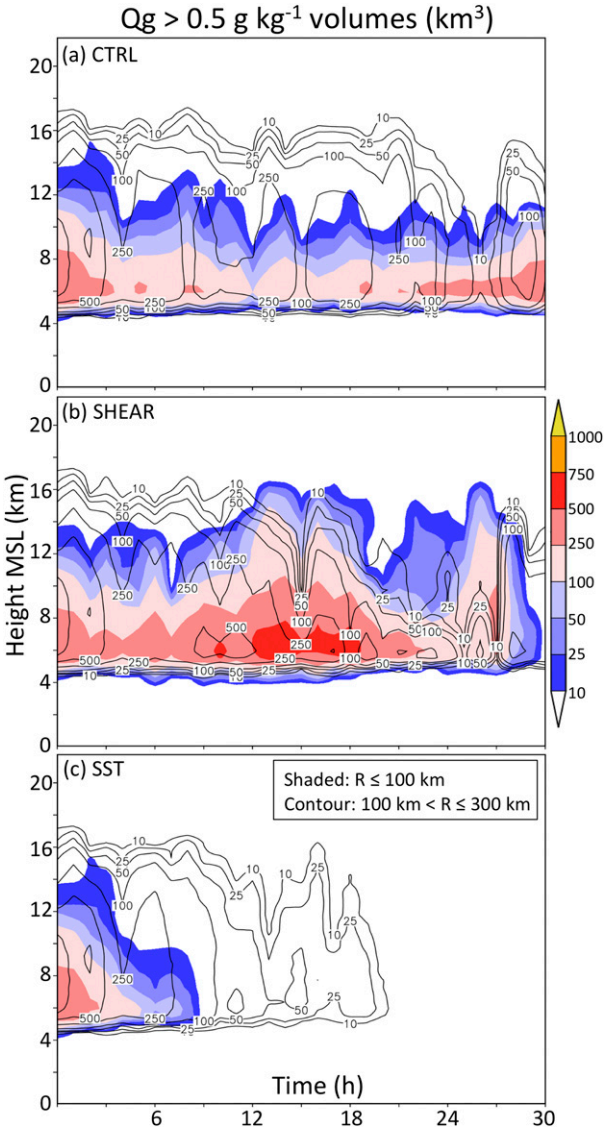

FIG. 10. As in Fig. 6, but for the 0.5 g kg^{-1} graupel volumes (km^3 per average level).

and detrained into the anvil cloud, while most of the negative charge on graupel will settle to lower levels. Because graupel tends to charge positively at warmer ambient temperatures (Figs. 1a, 12a), the charge separated on graupel reverses from negative at midlevels to positive below ~8 km down to ~6.5 km. In this simulation, the inductive charging rates (graupel–droplet; not shown) were generally one order of magnitude smaller than noninductive rates, as seen in previous studies using double-moment microphysics (e.g., Mansell et al. 2010; Fierro et al. 2015).

Differences in simulated bulk electrical structures between the inner core and the outer region of CTRL are highlighted by selected cross sections through representative lightning-active regions (Fig. 13). The noticeably shallower and less vigorous convection in the inner core is characterized by (i) shallower 30-dBZ echo tops (11 vs 14 km; Figs. 13a,b), (ii) smaller graupel mass mixing ratio (by ~2 g kg^{-1}) with the maximum contours generally located at lower levels (7 vs 10 km; Figs. 13a,b), and (iii) weaker vertical velocities (by ~5 m s^{-1}) rooted at lower levels (Figs. 13c,d). The weaker and shallower updrafts in the inner core are related to generally low cloud water content (CWC) above the freezing level (Figs. 13c,d) consistent with the conceptual model of Black and Hallett (1999). The high CWC values

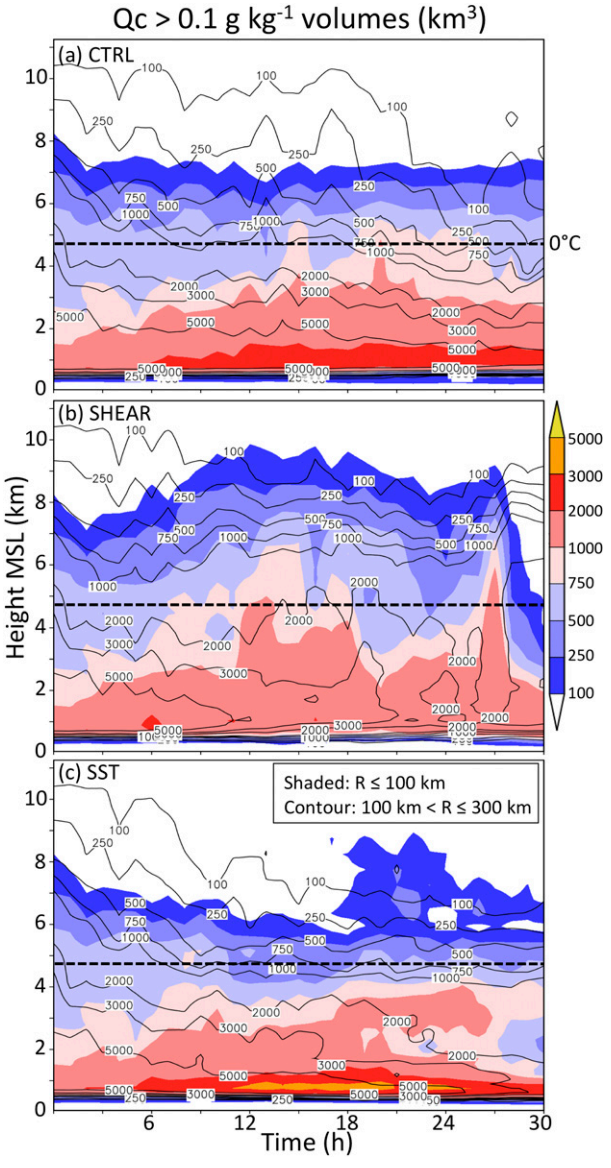

FIG. 11. As in Fig. 6, but for the 0.1 g kg^{-1} cloud water volumes (km^3 per average level). Note that the top of the vertical axis extends only up to z = 11.3 km MSL, compared to z = 22 km MSL in all other volume plots. For reference, the approximate height of the 0°C isotherm (domainwide) is shown by a dashed black horizontal line.

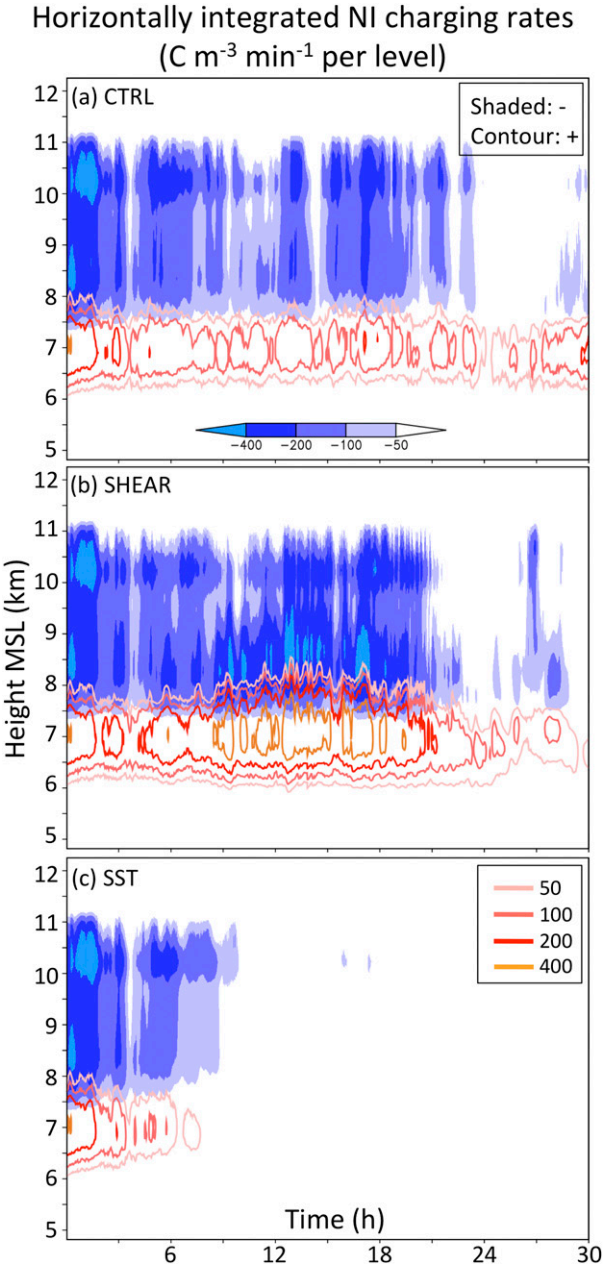

FIG. 12. Time–height diagram of the horizontally integrated graupel–cloud ice + graupel–snow noninductive charging rates (C m^{-3} min^{-1} per average level) throughout the entire simulation domain zoomed over $z \approx$ 5–12 km MSL for (a) CTRL, (b) SHEAR, and (c) SST. Legends for contours (positive rates) and shading (negative rates) are shown in (c) and (a), respectively. As in Fig. 6, the contour levels were set to be the same as for the shading to facilitate comparison. This plot uses 1-min time–height data, in contrast to the hourly model output data used for all other time–height plots.

below 2 km in the inner-core updrafts are quickly depleted during ascent by active coalescence and accretion by rain, as seen in larger rain content in the inner core below the freezing level (near 5 km; Figs. 13c,d). This is in contrast to the outer-band example, where appreciable CWC ($\geq$0.1 g m^{-3}) is found up to −30°C. The larger graupel mass coupled with higher CWC in the 0 to −30°C layer in the outer-band convection accounts for larger volumes of noninductive charging rates ($\geq$1 nC m^{-3} s^{-1}; Figs. 13a,b) and larger volumes of moderate net charge of either polarity aloft ($\rho \geq$ 0.1 nC m^{-3}; Figs. 13c,d).

Consistent with Fig. 7, the convection in the outer region in CTRL exhibits a more prominent upper positive charge region (near −30°C) along with a main midlevel negative charge region that extends to higher

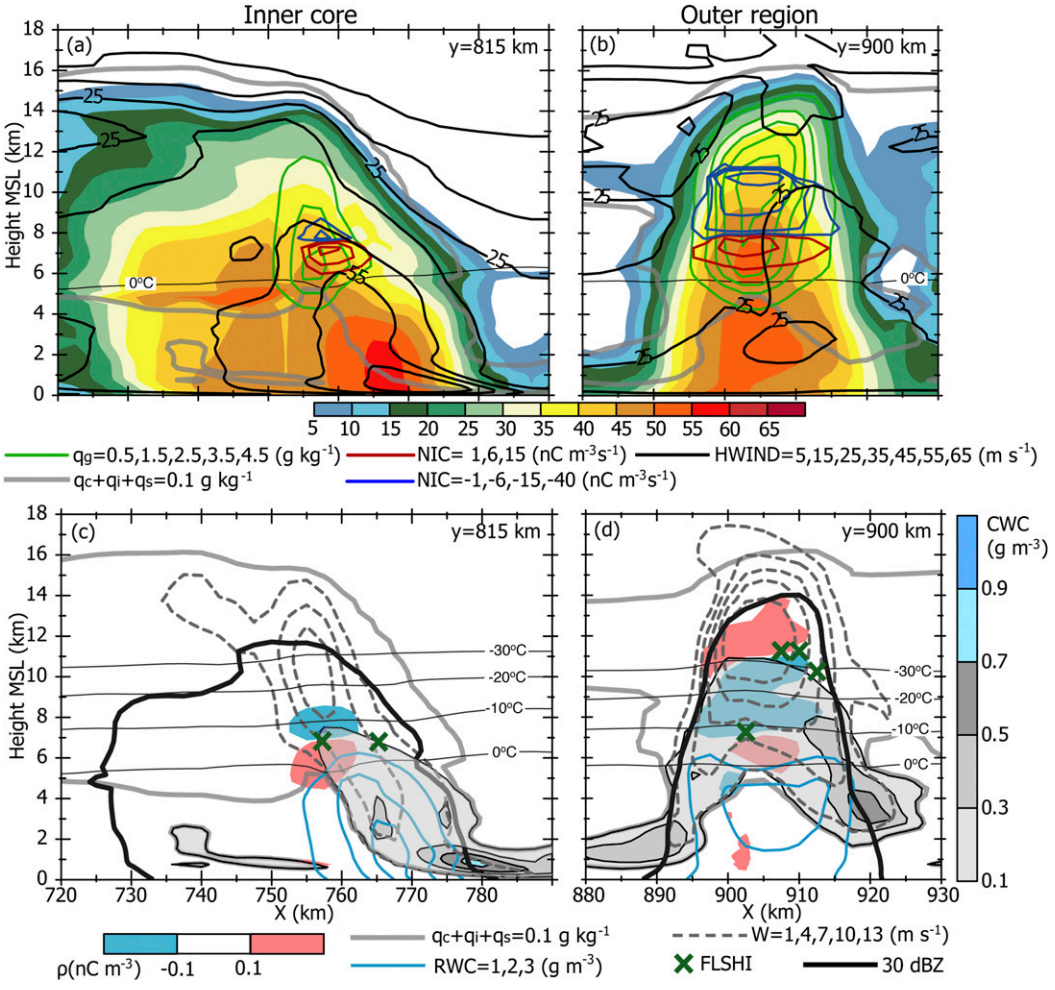

FIG. 13. East–west cross sections of electrical, microphysical, and kinematic variables at $t = 3$ h across representative sections of (a),(c) the eyewall and (b),(d) the outer region for CTRL. (a),(b) Radar reflectivity fields (shaded) overlaid with graupel mass mixing ratio q_g (g kg^{-1}; green contours), horizontal wind speed (HWIND; m s^{-1}; black contours), net noninductive charging rate [nC m^{-3} s^{-1}; red (positive) and blue (negative) contours]. (c),(d) The net charge density ρ (nC m^{-3}; blue and red shading), CWC (g m^{-3}; gray and blue shading) vertical velocity w (m s^{-1}; dashed gray contours), 30-dBZ echo outline (thick black contour), flash initiation locations (FLSHI; green crosses), and rainwater content (RWC; g m^{-3}; blue contours). The cloud outline, depicted by the 0.1 g kg^{-1} contour of the sum of cloud mixing ratio q_c, ice mixing ratio q_i, and snow mixing ratio q_s, is also shown in all panels for reference.

levels (Figs. 13c,d). The inner core, in contrast, exhibits a weaker negative charge region (Figs. 13c,d) and less upper positive charge. As illustrated in Figs. 13a and 13b, this arises from the lack of CWC above the −10°C isotherm in the inner-core region. At the locations of the cross sections in Fig. 13, the inner core exhibits a low, inverted dipole charge structure, while the convection in the outer region is characterized by a normal tripole. Although not shown in Fig. 13a, weaker positive charge ($\rho < 0.1$ nC m^{-3}) exists above −15°C, which would then classify the charge structure in the inner core as a bottom-heavy tripole, in line with the volume plots in Fig. 7. The larger volumes of appreciable ($\rho \geq 0.1$ nC m^{-3}) positive charge at upper levels in the outer region account for the larger production of lightning discharges there (Figs. 13c,d), while the generally comparable volumes of charge below 7 km explain that both regions produce fewer flashes at lower levels. As shown in Fig. 7 and illustrated in Figs. 13c and 13d, the vast majority of the flashes produced in the outer region (Fig. 2a) initiate at the charge interface at upper levels (~10.5 km) because of the dominant negative charging of graupel. The positive electrical potential (not shown) associated with the lower positive charge region in the inner core is stronger relative to the negative potential magnitude at midlevels compared to the outer region.

Consistent with Mansell et al. (2010), these respective vertical potential configurations would favor IC flash production at lower levels in the inner core, while favoring CG flash production in the outer region.

b. *SHEAR experiment*

Motivated by previous observational studies showing a relationship between eyewall lightning and shear magnitude/direction (e.g., Corbosiero and Molinari 2002; Abarca et al. 2011; Stevenson et al. 2016), SHEAR attempts to broadly replicate observations to shed insights on some of the main differences in electrical structures between a sheared storm and a steady-state major axisymmetric TC (i.e., CTRL). The imposed strong full-tropospheric shear is unidirectional and positive in the zonal direction (i.e., $\Delta U = +15\,\mathrm{m\,s^{-1}}$ increase in 10 h between ~850 and 250 hPa). Because the vortex is nearly stationary (translation speed $\leq 2\,\mathrm{m\,s^{-1}}$), the upshear (downshear) semicircle is located on the left (right), respectively.

Consistent with observations, the introduction of strong deep wind shear results in a notable weakening of the TC with a minimum surface pressure rising from about 942 hPa at the beginning of the simulation to about 985 hPa 30 h later (Fig. 2b). The time series of hourly flash rates in Fig. 2b reveals a salient difference with respect to CTRL (Fig. 2a): namely, a noticeable increase in inner-core lightning starting ~5 h into the simulation (and ending at 23 h) with rates ranging between 50 and 300 flashes $\mathrm{h^{-1}}$. Between hours 10 and 23, the inner-core flash rates systematically exceed those occurring in the outer region (cf. gray and black portions of the bars in Fig. 2b). In contrast to CTRL, the sheared TC produced some CG flashes lowering positive charge (+CGs) and produced nearly 7 times more −CGs than CTRL, most of which were located in the inner core (Fig. 2b and see later in the section).

The spatial distribution of the 30-h accumulated lightning discharges in the inner-core region (Fig. 3) reveals an unambiguous maximum in the downshear left quadrant with about 84% of the inner-core flashes. This result is consistent with the spatial patterns of CG flashes in observed TCs (e.g., Corbosiero and Molinari 2002; Abarca et al. 2011). The outer region produced a lightning pattern similar to CTRL with about 50% of the flashes located in the downshear right quadrant (Fig. 3).

Horizontal cross sections (Fig. 4b,e) and a Hovmöller diagram (Fig. 5b) of the simulated reflectivity fields and 1-h accumulated lightning fields further highlight the stark differences relative to CTRL in terms of the relationship between precipitating hydrometeor fields and lightning locations. Figure 4b shows that the inner-core lightning for SHEAR remains generally clustered near a well-defined maximum in reflectivity exceeding 55 dBZ in the downshear left quadrant of a progressively more open eyewall, which also exhibits a well-defined wavenumber-1 reflectivity pattern, consistent with observational (e.g., Marks et al. 1992; Reasor et al. 2000) and modeling work (e.g., Rogers et al. 2003).

As time progresses (cf. Figs. 4b and 4e), the rainband convection in SHEAR develops into a well-defined comma shape south of the inner-core region. North of the inner-core region, the enhanced convection in the northern semicircle (i.e., upshear and downshear left quadrants), coupled with rearward and azimuthal advection (i.e., eastward and northward) of hydrometeors, accounts for the formation of a prominent area of precipitation (Fig. 4e). These are typical features of extratropical systems (e.g., Bluestein 1992) or TCs undergoing extratropical transition (e.g., Davis et al. 2008; Foerster et al. 2014). The Hovmöller diagram (Fig. 5b) further highlights how the eyewall becomes more ill-defined while developing a maximum in lightning near the 35–40-km radius between hours 6 and 18. The progressive reduction in lightning activity with time in the outer region first documented in Fig. 2b becomes also evident in Fig. 5b. By about 22 h of simulation, the storm has been completely torn apart by the strong shear (Fig. 5b).

Time–height volume plots for the inner core and the outer region reveal notable contrasts with respect to CTRL that account for the lightning patterns (Figs. 3 and 4b,e) and evolution (Fig. 2b) described earlier. In line with heightened lightning activity in the asymmetric inner core between hours 10 and 23 (Figs. 2b, 4b,e, and 5b), the total channel volumes are noticeably larger than in the outer region during that period. Akin to CTRL, the lightning channel volumes in the inner core systematically extend to lower levels (4–8 km) compared to the outer region, especially during the aforementioned period. The significantly larger volumes of channels at even lower levels compared to CTRL (i.e., below 4 km) are consistent with the production of noticeably more CG flashes in SHEAR.

The relatively larger lightning production in the inner core than the outer region between hours 10 and 23 in SHEAR is associated with larger and deeper contours of $|0.1|\,\mathrm{nC\,m^{-3}}$ space charge density volumes (Fig. 8b), $5\,\mathrm{m\,s^{-1}}$ updraft volumes (Fig. 9b), and $0.5\,\mathrm{g\,kg^{-1}}$ graupel volumes (Fig. 10b). This is consistent with the magnitude of the noninductive charging rate increasing as a function of graupel content (Fig. 1a; SP98) and with graupel content being contingent upon the presence of appreciable ($\geq 5\,\mathrm{m\,s^{-1}}$) vertical velocities (Zipser and Lutz 1994; Wiens et al. 2005; Kuhlman et al. 2006) and sufficient CWC. The respective maxima of these volumes are even comparable to those found in the outer region of CTRL (cf. with Figs. 6a, 8a, 9a, 10a, and 11a).

The inner core of SHEAR exhibits deeper 0.1 g kg^{-1} contours of cloud water volume above the freezing level (4.5–5 km) relative to CTRL, which are associated with a prominent area of weaker convective (<7 m s^{-1}; Figs. 4b,e, 9a,b) precipitation in the northern semicircle (Figs. 11a,b). This is consistent with larger graupel volumes (Figs. 10a,b) and, in turn, larger charge volumes (Figs. 8a,b) and lightning channel volumes there (Figs. 6a,b). Figures 11a and 11b also show that above about 9–10 km clouds are essentially glaciated, owing primarily to riming by ice hydrometeors.

The time–height diagram of domain-integrated net graupel noninductive charging rates (Fig. 12b) points toward a similar domainwide gross charge structure as in CTRL: namely, a normal tripole. This accounts for the result that the vast majority (96%) of all simulated CG flashes lowered negative charge. The gradual increase in inner-core lightning between hours 10 and 19 (Fig. 2b) is coincident in time with a notable relative increase in domain-integrated noninductive charging rates, especially below ~9.5 km (Fig. 12b).

Similar to CTRL (Fig. 13), Fig. 14 shows a representative cross section in the most lightning-active area of the inner-core region of SHEAR, located in the downshear left quadrant (Figs. 3, 4b). The microphysical and electrical structure of the convection in the outer region is overall similar to that of CTRL (not shown).

The inner-core updrafts are somewhat weaker than in some of the individual, smaller-scale convective elements in the outer region (Figs. 13d, 14b). The downshear left quadrant of the SHEAR inner core exhibits, however, moderate vertical velocities ($w \geq 5$ m s^{-1}), graupel mass mixing ratios ($q_g \geq 3$ g kg^{-1}), and CWC (≥0.1 g m^{-3}) over a significantly larger grid volume than in the outer region (Figs. 9b, 10b). Also, the convection in the outer region is episodic, while, in contrast, the shear-induced convection in the downshear left quadrant of the inner core persists for more than 12 h (Figs. 9b, 10b). Observational work of Reasor et al. (2009) showed that such convective invigoration in the eyewall of sheared hurricanes arose from shear-forced mesoscale ascent in the downshear eyewall modulated by internally generated vorticity asymmetries. These factors combine to account for the persistence of larger volumes of moderate noninductive charging rates (≥1 nC m^{-3} s^{-1}) (Fig. 14a) and, consequently, volumes of charge in the inner core (Fig. 14b). Because the volume of negative charge at midlevels in the inner core of SHEAR is even larger than in the outer region of CTRL (Figs. 8a, b and 12a, b), its normal tripole charge structure produces larger volumes of high electric field magnitudes (i.e., ≥100 kV m^{-1}; not shown), yielding larger lightning production at both charge interfaces of the tripole (cf. Fig. 13d, 14b). Similar to the outer region in CTRL, the inner core of the sheared TC exhibits a positive electric potential (not shown) at low levels that is markedly weaker than the negative potential magnitude at midlevels. These factors account for the larger −CG flash production in the inner core of SHEAR relative to the outer region of CTRL (Figs. 2a,b, 3) (Mansell et al. 2010).

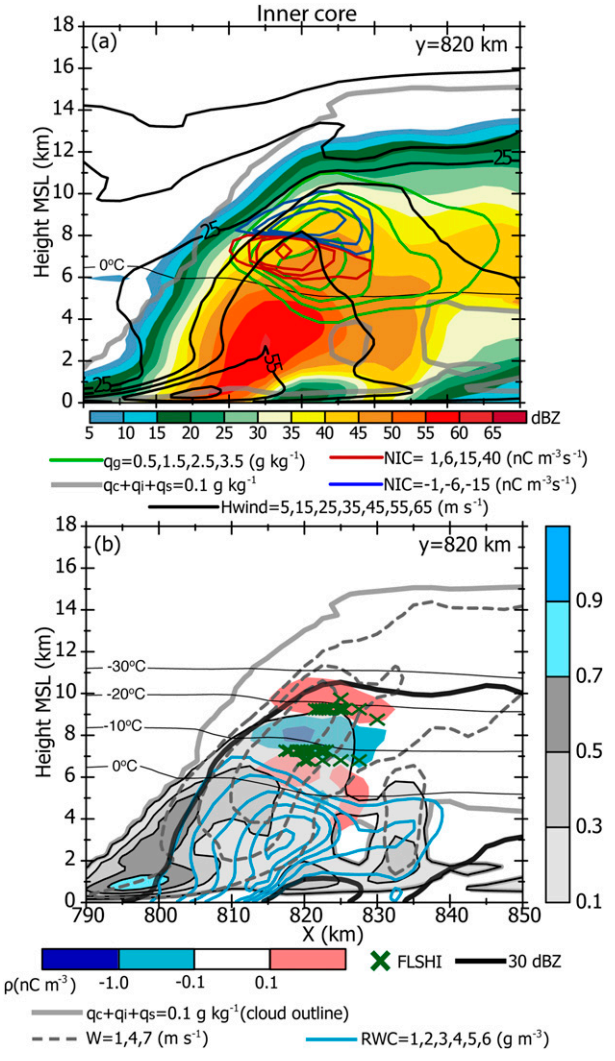

FIG. 14. As in Fig. 13, but for a representative section of the inner-core convection at t = 9h for SHEAR.

c. *SST experiment*

This last experiment was designed to illustrate how a TC exhibiting a weakening rate similar to SHEAR yields notable differences in electrical structures and evolution. As anticipated, reducing the SST from an initial value of 27°C down to 22°C results in a progressive weakening of the vortex (Fig. 2c). The filling rate is

remarkably similar to that of SHEAR: namely, an increase from an initial minimum surface pressure of about 942 to about 982 hPa at the end of the simulation (cf. Fig. 2b and 2c). The time series of lightning flash rates (Fig. 2c) shows a dearth of lightning after about hour 10. The quadrant distribution of the 30-h accumulated lightning discharges in both the inner-core and outer regions (Fig. 3) is similar to CTRL and is attributed to the first 10 h of simulation wherein the two solutions exhibit the smallest departure from each other.

The sharp reduction in sea surface moisture and heat fluxes results in an inner core characterized by overall smaller reflectivity values than either CTRL or SHEAR, generally by about 10–15 dBZ after about 10 h. This is clearly seen in the Hovmöller space (Fig. 5c), which also reveals a progressive reduction of 30-dBZ echo tops before the inner-core convection eventually collapses by about hour 24.

Despite a nearly identical weakening rate, the SHEAR and SST experiments exhibit stark differences in their bulk electrical and microphysical structures, as evidenced in the SST run by markedly smaller volumes of total lightning channels (Fig. 6c), $|0.1|\,\mathrm{nC\,m^{-3}}$ charge densities (Fig. 8c), $5\,\mathrm{m\,s^{-1}}$ vertical velocities (Fig. 9c), and $0.5\,\mathrm{g\,kg^{-1}}$ graupel mass (Fig. 10c), along with much smaller net graupel noninductive charging rates (Fig. 12c). During most of the simulation, the weaker convection in the inner core of SST exhibits cloud water volumes above the freezing level that are generally lower than those of CTRL (Figs. 11a,c). This is consistent with the inner core of CTRL containing appreciably larger volumes of graupel and charge (Figs. 8a,c, 10a,c).

5. Conclusions

Using an explicit cloud-scale electrification model, this work investigates the differences in electrical structures and evolution of a strong axisymmetric hurricane-like vortex (CTRL) subjected to prescribed changes in sea surface temperature (SST) or wind shear (SHEAR). The SHEAR and SST cases had very similar rates of weakening (as measured by the minimum surface pressure) but very contrasting decay modes and lightning evolution.

The vast majority of the CG discharges in the simulations lowered negative charge, which was consistent with a normal tripole gross vertical charge structure in the inner core ($r \leq 100$ km) and outer region ($100 < r \leq 300$ km) in all three experiments. The steady-state, nearly axisymmetric vortex in CTRL produced the vast majority (~91%) of its lightning in the outer region, consistent with observations of steady-state strong TCs. The inner core in CTRL had overall weaker electrification relative to the outer region, as evidenced by comparatively smaller volumes of graupel, charge density, and moderate updraft speed ($5\,\mathrm{m\,s^{-1}}$). This result constitutes a noticeable improvement over earlier modeling works of Fierro and Reisner (2011) and Fierro et al. (2007, 2013, 2015) wherein their simulated TCs exhibited a systematic overestimation of graupel content (and, hence, lightning rates) in the inner core relative to the outer region.

Consistent with earlier observational works, the imposition of strong, deep westerly shear resulted in a well-defined wavenumber-1 asymmetry in radar reflectivity fields in the downshear left quadrant of the inner core. The enhanced shear-induced volume of mixed-phase precipitation in the downshear left quadrant of the inner core coincided with a noticeable increase in inner-core lightning with flash rates comparable to or even exceeding those found in the (weakened) outer-region convection. This increase in inner-core lightning was coincident with notable increases in $0.5\,\mathrm{g\,kg^{-1}}$ graupel volumes, $0.1\,\mathrm{g\,kg^{-1}}$ cloud water volumes above the freezing level, $5\,\mathrm{m\,s^{-1}}$ updraft volumes, and volumes of $0.1\,\mathrm{nC\,m^{-3}}$ charge density magnitudes.

In both SHEAR and CTRL, it was found that, overall, moderate updraft speeds ($5\,\mathrm{m\,s^{-1}}$) in the inner-core convection were located at noticeably lower levels (below 6 km) compared to the outer region. In CTRL, the cloud water in the shallower updrafts in the inner core (relative to the outer region) were rapidly depleted by active autoconversion and accretion (i.e., warm rain) processes, in turn confining the majority of the charging to a shallow layer above the freezing level. This resulted in the development of a bottom-heavy tripole charge structure. In SHEAR, the asymmetric inner core had updrafts that were generally deeper, owing to persistent dynamical forcing over a relatively broad area, which allowed larger amounts of cloud water and graupel to reside and persist in the 0° to −20°C layer. In contrast to the inner core in CTRL, SHEAR exhibited a more substantial negative charge layer relative to the lower levels, which accounts for the larger production of negative CGs in SHEAR.

Given that the current experimental design assumes an initial steady-state intense TC and, given the challenges in simulating a TC intensifying in a realistic manner in this idealized framework, future work will place emphasis on conducting a similar analysis for intensifying storms with focus on rapid intensification.

Acknowledgments. Funding was provided by NOAA/Office of Oceanic and Atmospheric Research under NOAA–University of Oklahoma Cooperative Agreement NA11OAR4320072, U.S. Department of Commerce. This

work was further supported by the National Oceanic and Atmospheric Administration (NOAA) of the U.S. Department of Commerce under Grant NOAA-OAR-CIPO-2014-2003893 and Grant NOAA-NWS-NWSPO-2016-2004610. The simulations were made possible through computing resources provided by NOAA (HPC "Jet") with auxiliary computing resources also provided by the Oklahoma Supercomputing Center for Education and Research (OSCER). The authors thank Mark DeMaria and John Knaff for their valuable discussions. Thanks also go out to Dave Jorgensen for providing insightful comments on an earlier version of this manuscript and Dave Nolan for helpful advice. The authors also would like to express their gratitude to Earle Williams and two anonymous reviewers for their contributions, which helped improve the quality of the manuscript.

REFERENCES

Abarca, S. F., K. L. Corbosiero, and D. Vollaro, 2011: The World Wide Lightning Location Network and convective activity in tropical cyclones. *Mon. Wea. Rev.*, **139**, 175–191, doi:10.1175/2010MWR3383.1.

Anthes, R. A., 2003: Hot towers and hurricanes: Early observations, theories, and models. *Cloud Systems, Hurricanes, and the Tropical Rainfall Measuring Mission (TRMM)*, *Meteor. Monogr.*, No. 29, Amer. Meteor. Soc., 139–148, doi:10.1175/0065-9401(2003)029<0139:CHTAHE>2.0.CO;2.

Bigg, E. K., 1953: The formation of atmospheric ice crystals by the freezing of droplets. *Quart. J. Roy. Meteor. Soc.*, **79**, 510–519, doi:10.1002/qj.49707934207.

Black, R. A., and J. Hallett, 1999: Electrification of the hurricane. *J. Atmos. Sci.*, **56**, 2004–2028, doi:10.1175/1520-0469(1999)056<2004:EOTH>2.0.CO;2.

Bluestein, H. B., 1992: *Principles of Kinematics and Dynamics*. Vol. 1, *Synoptic-Dynamic Meteorology in Midlatitudes: Principles of Kinematics and Dynamics*, Oxford University Press, 431 pp.

Bovalo, C., C. Barthe, N. Yu, and N. Bègue, 2014: Lightning activity within tropical cyclones in the South West Indian Ocean. *J. Geophys. Res. Atmos.*, **119**, 8231–8244, doi:10.1002/2014JD021651.

Brooks, I. M., C. P. R. Saunders, R. P. Mitzeva, and S. L. Peck, 1997: The effect on thunderstorm charging of the rate of rime accretion by graupel. *Atmos. Res.*, **43**, 277–295, doi:10.1016/S0169-8095(96)00043-9.

Cecil, D. J., and E. J. Zipser, 2002: Reflectivity, ice scattering, and lightning characteristics of hurricane eyewalls and rainbands. Part II: Intercomparison of observations. *Mon. Wea. Rev.*, **130**, 785–801, doi:10.1175/1520-0493(2002)130<0785:RISALC>2.0.CO;2.

——, ——, and S. W. Nesbitt, 2002: Reflectivity, ice scattering, and lightning characteristics of hurricane eyewalls and rainbands. Part I: Quantitative description. *Mon. Wea. Rev.*, **130**, 769–784, doi:10.1175/1520-0493(2002)130<0769:RISALC>2.0.CO;2.

Chisnell, R. F., and J. Latham, 1974: A stochastic model of ice particle multiplication by drop splintering. *Quart. J. Roy. Meteor. Soc.*, **100**, 296–308, doi:10.1002/qj.49710042504.

Chiu, C.-S., 1978: Numerical study of cloud electrification in an axisymmetric time-dependent cloud model. *J. Geophys. Res.*, **83**, 5025–5049, doi:10.1029/JC083iC10p05025.

Coniglio, M. C., D. J. Stensrud, and L. J. Wicker, 2006: Effects of upper-level shear on the structure and maintenance of strong quasi-linear mesoscale convective systems. *J. Atmos. Sci.*, **63**, 1231–1252, doi:10.1175/JAS3681.1.

Corbosiero, K. L., and J. Molinari, 2002: The effects of vertical wind shear on the distribution of convection in tropical cyclones. *Mon. Wea. Rev.*, **130**, 2110–2123, doi:10.1175/1520-0493(2002)130<2110:TEOVWS>2.0.CO;2.

Davis, C. A., S. C. Jones, and M. Riemer, 2008: Hurricane vortex dynamics during Atlantic extratropical transition. *J. Atmos. Sci.*, **65**, 714–736, doi:10.1175/2007JAS2488.1.

DeMaria, M., R. T. DeMaria, J. A. Knaff, and D. Molenar, 2012: Tropical cyclone lightning and rapid intensity change. *Mon. Wea. Rev.*, **140**, 1828–1842, doi:10.1175/MWR-D-11-00236.1.

Dendy, J. E., Jr., 1982: Black box multigrid. *J. Comput. Phys.*, **48**, 366, doi:10.1016/0021-9991(82)90057-2.

——, 1987: Two multigrid methods for three-dimensional problems with discontinuous and anisotropic coefficients. *SIAM J. Sci. Stat. Comput.*, **8**, 673–685, doi:10.1137/0908059.

Dwyer, J. R., 2003: A fundamental limit on electric fields in air. *Geophys. Res. Lett.*, **30**, 2055, doi:10.1029/2003GL017781.

Fierro, A. O., and J. M. Reisner, 2011: High resolution simulation of the electrification and lightning of Hurricane Rita during the period of rapid intensification. *J. Atmos. Sci.*, **68**, 477–494, doi:10.1175/2010JAS3659.1.

——, M. S. Gilmore, E. R. Mansell, L. J. Wicker, and J. M. Straka, 2006: Electrification and lightning in an idealized boundary-crossing supercell simulation of 2 June 1995. *Mon. Wea. Rev.*, **134**, 3149–3172, doi:10.1175/MWR3231.1.

——, L. M. Leslie, E. R. Mansell, J. M. Straka, D. R. MacGorman, and C. Ziegler, 2007: A high resolution simulation of the microphysics and electrification in an idealized hurricane-like vortex. *Meteor. Atmos. Phys.*, **98**, 13–33, doi:10.1007/s00703-006-0237-0.

——, X.-M. Shao, J. M. Reisner, J. D. Harlin, and T. Hamlin, 2011: Evolution of eyewall convective events as indicated by intracloud and cloud-to-ground lightning activity during the rapid intensification of Hurricanes Rita and Katrina. *Mon. Wea. Rev.*, **139**, 1492–1504, doi:10.1175/2010MWR3532.1.

——, E. R. Mansell, C. Ziegler, and D. R. MacGorman, 2013: The implementation of an explicit charging and discharge lightning scheme within the WRF-ARW Model: Benchmark simulations of a continental squall line, a tropical cyclone, and a winter storm. *Mon. Wea. Rev.*, **141**, 2390–2415, doi:10.1175/MWR-D-12-00278.1.

——, ——, D. R. MacGorman, and C. Ziegler, 2015: Explicitly simulated electrification and lightning within a tropical cyclone based on the environment of Hurricane Isaac (2012). *J. Atmos. Sci.*, **72**, 4167–4193, doi:10.1175/JAS-D-14-0374.1.

Foerster, A. M., M. M. Bell, P. A. Harr, and S. C. Jones, 2014: Observations of the eyewall structure of Typhoon Sinlaku (2008) during the transformation stage of extratropical transition. *Mon. Wea. Rev.*, **142**, 3372–3392, doi:10.1175/MWR-D-13-00313.1.

Goodman, S. J., and Coauthors, 2013: The GOES-R Geostationary Lightning Mapper (GLM). *Atmos. Res.*, **125–126**, 34–49, doi:10.1016/j.atmosres.2013.01.006.

Guimond, S. R., G. M. Heymsfield, and F. J. Turk, 2010: Multiscale observations of Hurricane Dennis (2005): The effects of hot towers on rapid intensification. *J. Atmos. Sci.*, **67**, 633–654, doi:10.1175/2009JAS3119.1.

Hendricks, E. A., M. T. Montgomery, and C. A. Davis, 2004: The role of "vortical" hot towers in the formation of Tropical

Cyclone Diana (1984). *J. Atmos. Sci.*, **61**, 1209–1232, doi:10.1175/1520-0469(2004)061<1209:TROVHT>2.0.CO;2.

Kelley, O. A., J. Stout, and J. B. Halverson, 2004: Tall precipitation cells in tropical cyclone eyewalls are associated with tropical cyclone intensification. *Geophys. Res. Lett.*, **31**, L24112–L24115, doi:10.1029/2004GL021616.

Khain, A., V. Phillips, N. Benmoshe, and A. Pokrovsky, 2012: The role of small soluble aerosols in the microphysics of deep maritime clouds. *J. Atmos. Sci.*, **69**, 2787–2807, doi:10.1175/2011JAS3649.1.

——, B. Lynn, and J. Shpund, 2015: High resolution WRF simulations of hurricane Irene: Sensitivity to aerosols and choice of microphysical schemes. *Atmos. Res.*, **164**, 129–145, doi:10.1016/j.atmosres.2015.07.014.

Klemp, J. B., and R. B. Wilhelmson, 1978: The simulation of three-dimensional convective storm dynamics. *J. Atmos. Sci.*, **35**, 1070–1096, doi:10.1175/1520-0469(1978)035<1070:TSOTDC>2.0.CO;2.

Kuhlman, K. M., C. L. Ziegler, E. R. Mansell, D. R. MacGorman, and J. M. Straka, 2006: Numerically simulated electrification and lightning of the 29 June 2000 STEPS supercell storm. *Mon. Wea. Rev.*, **134**, 2734–2757, doi:10.1175/MWR3217.1.

Lang, T. J., and S. A. Rutledge, 2002: Relationships between convective storm kinematics, precipitation, and lightning. *Mon. Wea. Rev.*, **130**, 2492–2506, doi:10.1175/1520-0493(2002)130<2492:RBCSKP>2.0.CO;2.

Lawson, R. P., S. Woods, and H. Morrison, 2015: The microphysics of ice and precipitation development in tropical cumulus clouds. *J. Atmos. Sci.*, **72**, 2429–2445, doi:10.1175/JAS-D-14-0274.1.

Letkewicz, C. E., A. J. French, and M. D. Parker, 2013: Base-state substitution: An idealized modeling technique for approximating environmental variability. *Mon. Wea. Rev.*, **141**, 3062–3086, doi:10.1175/MWR-D-12-00200.1.

Lyons, W. A., M. G. Venne, P. G. Black, and R. C. Gentry, 1989: Hurricane lightning: A new diagnostic tool for tropical storm forecasting? Preprints, *18th Conf. on Hurricanes and Tropical Meteorology*, San Diego, CA, Amer. Meteor. Soc., 113–114.

MacGorman, D. R., and W. D. Rust, 1998: *The Electrical Nature of Storms*. Oxford University Press, 422 pp.

——, D. W. Burgess, V. Mazur, W. D. Rust, W. L. Taylor, and B. C. Johnson, 1989: Lightning rates relative to tornadic storm evolution on 22 May 1981. *J. Atmos. Sci.*, **46**, 221–251, doi:10.1175/1520-0469(1989)046<0221:LRRTTS>2.0.CO;2.

Mansell, E. R., and C. L. Ziegler, 2013: Aerosol effects on simulated storm electrification and precipitation in a two-moment bulk microphysics model. *J. Atmos. Sci.*, **70**, 2032–2050, doi:10.1175/JAS-D-12-0264.1.

——, D. R. MacGorman, C. L. Ziegler, and J. M. Straka, 2002: Simulated three-dimensional branched lightning in a numerical thunderstorm model. *J. Geophys. Res.*, **107**, doi:10.1029/2000JD000244.

——, ——, ——, and ——, 2005: Charge structure and lightning sensitivity in a simulated multicell storm. *J. Geophys. Res.*, **110**, D12101, doi:10.1029/2004JD005287.

——, C. L. Ziegler, and C. Bruning, 2010: Simulated electrification of a small thunderstorm with two-moment bulk microphysics. *J. Atmos. Sci.*, **67**, 171–194, doi:10.1175/2009JAS2965.1.

Marks, F. D., Jr., R. A. Houze Jr., and J. F. Gamache, 1992: Dual-aircraft investigation of the inner core of Hurricane Norbert. Part I: Kinematic structure. *J. Atmos. Sci.*, **49**, 919–942, doi:10.1175/1520-0469(1992)049<0919:DAIOTI>2.0.CO;2.

Molinari, J., P. K. Moore, V. P. Idone, R. W. Henderson, and A. B. Saljoughy, 1994: Cloud-to-ground lightning in Hurricane Andrew. *J. Geophys. Res.*, **99**, 16 665–16 676, doi:10.1029/94JD00722.

——, ——, and ——, 1999: Convective structure of hurricanes as revealed by lightning locations. *Mon. Wea. Rev.*, **127**, 520–534, doi:10.1175/1520-0493(1999)127<0520:CSOHAR>2.0.CO;2.

Montgomery, M. T., M. E. Nicholls, T. A. Cram, and A. B. Saunders, 2006: A vortical hot tower route to tropical cyclogenesis. *J. Atmos. Sci.*, **63**, 355–386, doi:10.1175/JAS3604.1.

Nolan, D. S., Y. Moon, and D. P. Stern, 2007: Tropical cyclone intensification from asymmetric convection: Energetics and efficiency. *J. Atmos. Sci.*, **64**, 3377–3405, doi:10.1175/JAS3988.1.

Orville, R. E., and J. M. Coyne, 1999: Cloud-to-ground lightning in tropical cyclones (1986–1996). Preprints, *23rd Conf. on Hurricanes and Tropical Meteorology*, Dallas, TX, Amer. Meteor. Soc., 4A.12. [Available online at https://ams.confex.com/ams/older/99annual/abstracts/1695.htm.]

Phillips, V. T. J., L. J. Donner, and S. T. Garner, 2007: Nucleation processes in deep convection simulated by a cloud-system-resolving model with double-moment bulk microphysics. *J. Atmos. Sci.*, **64**, 738–761, doi:10.1175/JAS3869.1.

Powell, M. D., P. J. Vickery, and T. A. Reinhold, 2003: Reduced drag coefficient for high wind speeds in tropical cyclones. *Nature*, **422**, 279–283, doi:10.1038/nature01481.

Price, C., M. Asfur, and Y. Yair, 2009: Maximum hurricane intensity preceded by increase in lightning frequency. *Nat. Geosci.*, **2**, 329–332, doi:10.1038/ngeo477.

Reasor, P. D., M. T. Montgomery, F. D. Marks, and J. F. Gamache, 2000: Low-wavenumber structure and evolution of the hurricane inner core observed by airborne dual-Doppler radar. *Mon. Wea. Rev.*, **128**, 1653–1680, doi:10.1175/1520-0493(2000)128<1653:LWSAEO>2.0.CO;2.

——, M. D. Eastin, and J. F. Gamache, 2009: Rapidly intensifying Hurricane Guillermo (1997). Part I: Low-wavenumber structure and evolution. *Mon. Wea. Rev.*, **137**, 603–631, doi:10.1175/2008MWR2487.1.

Rogers, R. F., S. Chen, J. Tenerelli, and H. Willoughby, 2003: A numerical study of the impact of vertical shear on the distribution of rainfall in Hurricane Bonnie (1998). *Mon. Wea. Rev.*, **131**, 1577–1599, doi:10.1175//2546.1.

Rotunno, R., and K. A. Emanuel, 1987: An air–sea interaction theory for tropical cyclones. Part II: Evolutionary study using a nonhydrostatic axisymmetric numerical model. *J. Atmos. Sci.*, **44**, 542–561, doi:10.1175/1520-0469(1987)044<0542:AAITFT>2.0.CO;2.

Samsury, C. E., and R. E. Orville, 1994: Cloud-to-ground lightning in tropical cyclones: A study of Hurricanes Hugo (1989) and Jerry (1989). *Mon. Wea. Rev.*, **122**, 1887–1896, doi:10.1175/1520-0493(1994)122<1887:CTGLIT>2.0.CO;2.

Saunders, C. P. R., and L. S. Peck, 1998: Laboratory studies of the influence of the rime accretion rate on charge transfer during crystal–graupel collisions. *J. Geophys. Res.*, **103**, 13 949–13 956, doi:10.1029/97JD02644.

Schultz, C. J., W. A. Petersen, and L. D. Carey, 2011: Lightning and severe weather: A comparison between total and cloud-to-ground lightning trends. *Wea. Forecasting*, **26**, 744–755, doi:10.1175/WAF-D-10-05026.1.

Shao, X. M., and Coauthors, 2005: Katrina and Rita were lit up with lightning. *Eos, Trans. Amer. Geophys. Union*, **86**, 398, doi:10.1029/2005EO420004.

Shapiro, L. J., 1983: The asymmetric boundary layer flow under a translating hurricane. *J. Atmos. Sci.*, **40**, 1984–1998, doi:10.1175/1520-0469(1983)040<1984:TABLFU>2.0.CO;2.

——, and J. L. Franklin, 1999: Potential vorticity asymmetries and tropical cyclone motion. *Mon. Wea. Rev.*, **127**, 124–131, doi:10.1175/1520-0493(1999)127<0124:PVAATC>2.0.CO;2.

Skamarock, W. C., and J. B. Klemp, 2008: A time-split nonhydrostatic atmospheric model for weather research and forecasting applications. *J. Comput. Phys.*, **227**, 3465–3485, doi:10.1016/j.jcp.2007.01.037.

Squires, K., and S. Businger, 2008: The morphology of eyewall lightning outbreaks in two category 5 hurricanes. *Mon. Wea. Rev.*, **136**, 1706–1726, doi:10.1175/2007MWR2150.1.

Stevenson, S. N., K. L. Corbosiero, and S. F. Abarca, 2016: Lightning in eastern North Pacific tropical cyclones: A comparison to the North Atlantic. *Mon. Wea. Rev.*, **144**, 225–239, doi:10.1175/MWR-D-15-0276.1.

Thomas, J. N., N. Solorzano, S. A. Cummer, and R. H. Holzworth, 2010: Polarity and energetics of inner core lightning in three intense North Atlantic hurricanes. *J. Geophys. Res.*, **115**, A00E15, doi:10.1029/2009JA014777.

Twomey, S., 1959: The nuclei of natural cloud formation. Part II: The supersaturation in natural clouds and the variation of cloud droplet concentration. *Geofis. Pura Appl.*, **43**, 243–249, doi:10.1007/BF01993560.

Wicker, L. J., and R. B. Wilhelmson, 1995: Simulation and analysis of tornado development and decay within a three-dimensional supercell thunderstorm. *J. Atmos. Sci.*, **52**, 2675–2703, doi:10.1175/1520-0469(1995)052<2675:SAAOTD>2.0.CO;2.

Wiens, K. C., S. A. Rutledge, and S. A. Tessendorf, 2005: The 29 June 2000 supercell observed during STEPS. Part II: Lightning and charge structure. *J. Atmos. Sci.*, **62**, 4151–4177, doi:10.1175/JAS3615.1.

Williams, E. R., 1989: The tripole structure of thunderstorms. *J. Geophys. Res.*, **94**, 13 151–13 167, doi:10.1029/JD094iD11p13151.

——, 1995: Meteorological aspects of thunderstorms. *Handbook of Atmospheric Electrodynamics*, H. Volland, Ed., Vol. I, CRC Press, 27–60.

——, and N. Renno, 1993: An analysis of the conditional instability of the tropical atmosphere. *Mon. Wea. Rev.*, **121**, 21–36, doi:10.1175/1520-0493(1993)121<0021:AAOTCI>2.0.CO;2.

Ziegler, C. L., 1985: Retrieval of thermal and microphysical variables in observed convective storms. Part I: Model development and preliminary testing. *J. Atmos. Sci.*, **42**, 1487–1509, doi:10.1175/1520-0469(1985)042<1487:ROTAMV>2.0.CO;2.

——, D. R. MacGorman, J. E. Dye, and P. S. Ray, 1991: A model evaluation of noninductive graupel-ice charging in the early electrification of a mountain thunderstorm. *J. Geophys. Res.*, **96**, 12 833–12 855, doi:10.1029/91JD01246.

Zipser, E. J., and K. R. Lutz, 1994: The vertical profile of radar reflectivity of convective cells: A strong indicator of storm intensity and lightning probability? *Mon. Wea. Rev.*, **122**, 1751–1759, doi:10.1175/1520-0493(1994)122<1751:TVPORR>2.0.CO;2.